



High-resolution modeling study of an isolated convective storm over Seoul Metropolitan area

Young-Hee Lee¹ · Ki-Hong Min¹

Received: 14 March 2018 / Accepted: 6 January 2019 / Published online: 17 January 2019
© Springer-Verlag GmbH Austria, part of Springer Nature 2019

Abstract

The ability of a high-resolution (500 m) Weather Research and Forecasting (WRF) model to simulate an isolated convective precipitation event over Seoul metropolitan area on August 16, 2015 was investigated. To understand the effects of micro- and mesoscale forcing on the initiation of convective rainfall under large-scale conditions, we performed sensitivity tests using different initial times. Despite simulating the same case, the quantitative precipitation forecast and the timing of moist convection varied widely among the experiments. Mesoscale features such as outflow and low-level convergence are different in location and intensity among the experiments. When assimilation of surface observations and radar data was performed, the simulation reproduced the low-level convergence and, hence, the location and amount of rainfall reasonably well within the first 6 h of simulation period. The timing differences of convective rainfall among the experiments were examined in terms of the atmospheric boundary layer (ABL) growth. Rapid growth of the ABL enabled moist convection to occur early in the presence of an outflow. An overestimated maximum ABL height by the model also led to earlier collapse of the ABL as compared to observations, which contributed to a reduction of convective available potential energy over the urban area in late afternoon. The results of this study demonstrate that accurate simulation of ABL growth is important for predicting the timing and intensity of isolated convective storms.

1 Introduction

Flood damage in urban areas frequently occurs as a consequence of convective heavy rainfall that develops within a few hours during summer. The urban surface is mostly impervious (Arya 2001); hence, drainage of water can be problematic, which may lead to inundation of low-lying areas. Rainfall events associated with mid-latitude synoptic systems are relatively more predictable due to the long lifetime of the systems, but isolated convective rainfall events under high-pressure systems are short lived and less predictable (Lorenz 1969; Duran and Wyen 2016). Thus, predicting the location and intensity of convective rainfall events still remains a challenging problem. Uncertainty in both the initial conditions (ICs) and the physical processes contribute

to this limited predictability in numerical weather prediction models. To consider the uncertainty of ICs, ensemble model results with slightly different initial conditions have been used to predict convective precipitation probabilistically (Hanley et al. 2011; Walser et al. 2004). However, using such ensemble model results for very short-range (0–6 h) forecasting of rainfall is computationally expensive.

As computational speeds increase, it has become possible to simulate convection processes explicitly using a high-resolution numerical prediction model (e.g., Ducrocq et al. 2002; Davolio et al. 2007). However, high-resolution numerical prediction models are still inadequate for nowcasting of convective storms due to spin-up issues and the short lifetime of these storms. The typical spin-up period for a convection permitting model with cold start is 3–6 h, making the forecast in this period useless. After spin-up period, the models do not have good accuracy in storm location and timing (Sun et al. 2014). One way to reduce the spin-up period is to employ warm start initialization. For example, Zhang et al. (2006) found that increased model resolution improved the predictability of a convective rainfall event with data assimilation. Wang et al. (2013) showed that assimilation of

Responsible Editor: F. Mesinger.

✉ Young-Hee Lee
young@knu.ac.kr

¹ Department of Astronomy and Atmospheric Sciences,
Kyungpook National University, 80 Daehakro, Bukgu,
Daegu 41566, South Korea

radar reflectivity data significantly improved the short-term precipitation forecasting skill up to 7 h.

In South Korea, radar data assimilation research has a short history, since the availability of quality controlled radar data has become available in recent years (Lee et al. 2010; Min et al. 2015). There has been an increase in demand of such research because the Ministry of Land, Infrastructure, and Transportation (MOLIT) implemented a 6-year project (2014–2019) to install a small X-band radar network (X-Net) to complement the existing large S-band radars in Seoul metropolitan area. The goal of this project is to improve the nowcasting capabilities of urban area flash flooding and quantitative precipitation forecasts (QPF). This study was conducted in part to understand the impact of assimilating radar reflectivity data as ICs for simulating very short-range convective rainfall in Seoul city.

To improve the predictability of a convective rainfall event, it is also necessary to simulate the physical processes associated with convective rain reasonably. For deep convection to develop, a triggering mechanism is required along with conditional instability. Triggering mechanisms of upward motion include thermals within the atmospheric boundary layer (ABL), uplift along topography, ascent due to surface air convergence and others (Ahrens 2009). Several studies have investigated the initiation of summertime convective precipitation related to the growth of ABL (e.g., Findell and Eltahir 2003a, b; Juang et al. 2007; Yin et al. 2015). Juang et al. (2007) explored the triggers of convective precipitation for a wide range of soil moisture states and relative humidity of air and demonstrated the presence of a boundary line of relative humidity for the occurrence of convective precipitation for a given soil moisture state. In this study, we examine the timing and intensity of simulated moist convective precipitation in terms of ABL growth over an urban area.

The purposes of this study are to (1) investigate the ability of a high-resolution numerical prediction model with data assimilation to simulate isolated convective storms in the very short-term forecasting range and (2) examine the influence of ABL growth on the timing and intensity of convective precipitation through sensitivity tests.

2 Materials and methods

2.1 The model

The model used in this study is the Weather Research and Forecasting (WRF) V3.8 numerical model (Skamarock et al. 2008), which is a fully compressible non-hydrostatic atmospheric model. The numerical scheme uses third-order Runge–Kutta split-explicit time integration. Domain configuration consisted of four two-way nested grids

(Fig. 1a). Horizontal grid spacing was 13.5 km in domain 1 (80×80), 4.5 km in domain 2 (67×67), 1.5 km in domain 3 (106×121) and 0.5 km in domain 4 (139×106). There were 60 sigma vertical levels with model top at 50 hPa. The lateral boundary buffer zone was composed of five grid points, one point being specified and the remainder as a relaxation zone. The WRF single moment 6-class microphysics scheme (Hong and Lim 2006) and the Shin–Hong scale-aware planetary boundary layer parameterization schemes were used (Shin and Hong 2015). The longwave Rapid Radiation Transfer Model (RRTM, Mlawer et al. 1997) and the shortwave Dudhia scheme (Dudhia 1989) were selected

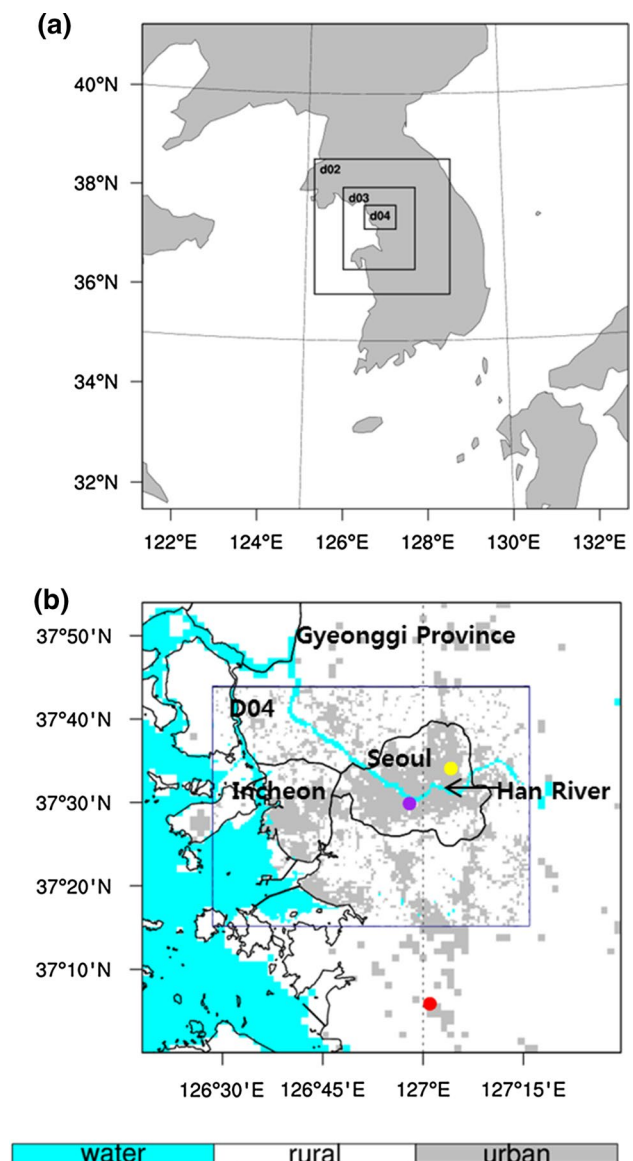


Fig. 1 **a** Domain configuration of the WRF, **b** horizontal distribution of urban and rural area in domain 4. Box in **b** indicates domain 4 and yellow, red, and purple circles indicate Jungnang site, Osan site, and Gwanak radar site, respectively

for the radiation processes. The Kain–Fritsch convective parameterization scheme (Kain and Fritsch 1993) was used for domains 1–3 and was turned off for domain 4 to explicitly simulate convection. The cumulus scheme was found to produce very little rainfall in domain 3. The land-surface model (LSM) was the Noah LSM (Mitchell 2005) using four-layer soil. Finally, a single-layer urban canopy model (Kusaka et al. 2001) was applied to characterize the metropolitan area. Figure 1b shows horizontal distribution of the urban area in domain 4 and its surrounding area. Domain 4 was heavily covered by urban areas and outside domain 4 was dominated by rural areas which consist of forest and farmland.

To examine the influence of micro- and mesoscale forcing on moist convection initiation in a given synoptic condition, we performed sensitivity tests with four different initial times (1200 and 1800 UTC on August 15, 2015 and 0000 and 0600 UTC on August 16, 2015). To investigate the applicability of the high-resolution WRF model in forecasting a convective storm in the very short-term forecasting range, a fifth experiment was performed commencing at 0600 UTC on August 16, 2015 using the assimilation of radar and ground-based observation as the initial conditions. Table 1 summarizes these experiments.

2.2 Data

Data used for the initial and boundary conditions of the WRF model were the National Centers for Environmental Prediction (NCEP) final (FNL) operational global analysis and forecast data (NCEP 2015). The horizontal resolution of the data was 0.25° with a time interval of 6 h. The land cover data used were 30-arc second data for the Korean Peninsula (Park and Suh 2015) and 3-arc second data for the Seoul Metropolitan area (NIMR 2014). The topography data used in this study were the USGS 30-arc second data for domains 1 and 2 and the Shuttle Radar Topography Mission (SRTM) 3-arc second data (Reuter et al. 2007) for domains 3 and 4.

To analyze the observational features of the study case, we used the surface weather map analyzed by the Korea Meteorological Administration (KMA), the sounding from

the Osan upper-level station ($37^\circ 6'N$, $127^\circ 1'48''E$), which is the closest to the Seoul metropolitan area (Fig. 1b), enhanced infrared imagery from the KMA Communication, Ocean, and Meteorology Satellite (COMS), and surface meteorological observations from the Automatic Weather Station (AWS) network of the KMA. For comparison with model results in domain 4, we used precipitation observations from the AWS.

Mixing height data (Park et al. 2017) obtained at Jungnang (JN) station ($37^\circ 34'48''N$, $127^\circ 4'46''E$) (Fig. 1b) were used for comparison with the simulated ABL height. The mixing height was determined using backscatter from ceilometer by applying the following procedures. Firstly, strong attenuated backscatter signals classified as cloud or rain drop were excluded (Munkel et al. 2007; Tsaknakis et al. 2011); secondly, the running mean for 11 point (11 min) and 11-point vertical (110 m) backscatter data were calculated to minimize the random noise error, and finally the mixing height was determined as the height with a minimum vertical gradient of attenuated backscatter from the ceilometer (Eresmaa et al. 2006).

2.3 Data assimilation methods

To examine the impact of data assimilation on the simulation of convective rainfall, we performed an experiment using the WRF data assimilation system. The 3-dimensional variational (3D-Var) data assimilation method in WRF is capable of assimilating all types of conventional observations as well as remote sensing data (Xiao and Sun 2007). The 3D-Var system combines observations with background information on the model state and uses a linearized forecast model to ensure that the observations are given a dynamically realistic and consistent analysis field. In this study, we used an incremental analysis update (IAU) WRF 3D-Var data assimilation system for storm-scale simulations (Barker et al. 2004, 2012; Lee et al. 2010).

The covariance matrix for the regional background error statistics was calculated using the National Meteorological Center method (Parrish and Derber 1992) by taking 24-h and 12-h forecasts during the summer period (June, July and August) for the chosen domain. Minimization of the cost function was performed using a conjugate gradient method. An hourly updated data assimilation cycle for 3 h was made. During each assimilation cycle, observations from radar reflectivity and radial velocity obtained from the KMA Gwanak radar site ($37^\circ 26'N$, $126^\circ 57'E$) and nearby AWS observations were used. Surface AWS data were used to augment the radar which was located approximately 640 m above ground level.

Table 1 Characteristics of numerical experiments

Experiment	Initial time	Data assimilation
IC12	1200 UTC on 15 Aug 2015	No
IC18	1800 UTC on 15 Aug 2015	No
IC00	0000 UTC on 16 Aug 2015	No
IC06	0600 UTC on 16 Aug 2015	No
IC06A	0600 UTC on 16 Aug 2015	Yes

2.4 Evaluation methods

The verification of a high-resolution rainfall simulation is not straightforward. As horizontal resolution increases, the model is able to produce more concentrated and intense rainfall. Small errors in location between observations and the simulation can produce large differences and consequently poor scores. Taking this into account, we performed model evaluation of rainfall amount over 5×5 km boxes rather than over 0.5×0.5 km grid. The AWS observations and model values were averaged over these 25 km² boxes. When only one AWS observation was available on a box, we assumed that rainfall at one AWS was representative of rainfall for the box. Precipitation bias error (BIAS) and root-mean square error (RMSE) were computed using the predicted versus observed precipitation in the innermost domain. Boxes with at least one AWS were used in the evaluation. The total number of boxes was 44, which represents about 30% of domain 4. The BIAS and RMSE were defined as;

$$\text{BIAS} = \frac{1}{N} \sum_{i=1}^N (P_i - O_i), \quad (1)$$

$$\text{RMSE} = \sqrt{\frac{1}{N} \sum_{i=1}^N (P_i - O_i)^2}, \quad (2)$$

where N is the number of boxes, and O_i and P_i are the observed and simulated value, respectively, at the i th box.

Based on a 2×2 contingency table (Table 2) established for the threshold, we computed the forecast accuracy (ACC), frequency bias (FBIAS), probability of detection (POD), false-alarm ratio (FAR), and Heidke skill score (HSS; e.g., Wilks 2006) as shown below;

$$\text{ACC} = \frac{a + d}{a + b + c + d} \quad (3)$$

$$\text{FBIAS} = \frac{b + d}{c + d}, \quad (4)$$

$$\text{POD} = \frac{d}{c + d}, \quad (5)$$

Table 2 Schematic 2×2 contingency table for the definition of scores

	$P_i < \text{threshold}$	$P_i \geq \text{threshold}$
$O_i < \text{threshold}$	a	b
$O_i \geq \text{threshold}$	c	d

O_i and P_i represents observation and prediction, respectively

$$\text{FAR} = \frac{b}{b + d}, \quad (6)$$

$$\text{HSS} = \frac{a + d - T}{a + b + c + d - T}, \quad (7)$$

where $T = [(a + b)(a + c) + (b + d)(c + d)] / (a + b + c + d)$ and refers to the expected number of all the correct predictions with a random forecast.

Verification was performed for 9-h accumulated rainfall at 1500 UTC on August 16, 2015. Domain 4 was covered by 56 AWS. We used 25 mm for the contingency table threshold (Table 2), which was the median value of observed rainfall of for the 44 analysis boxes.

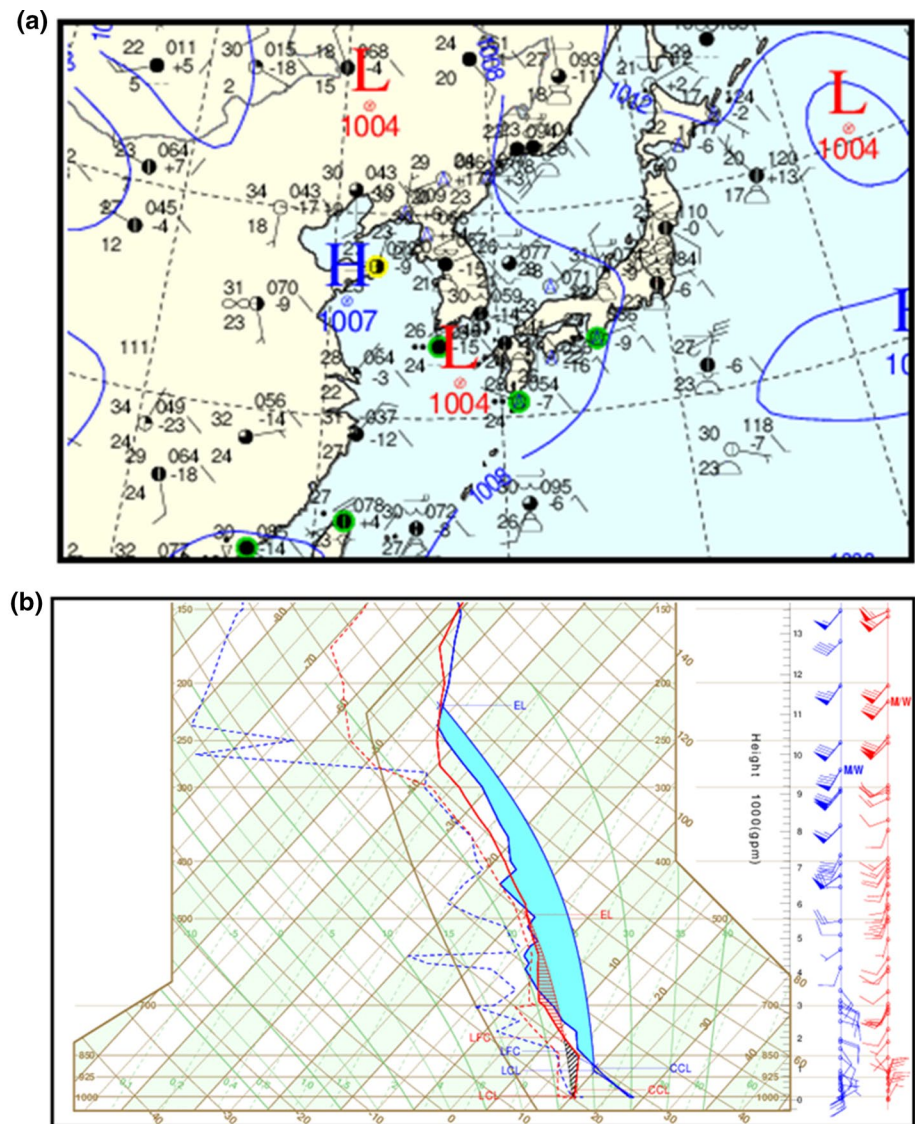
3 Observational analysis

The surface weather chart for 0600 UTC on August 16, 2015 shows very weak pressure gradient over the Korean peninsula with a high pressure system to the west (Fig. 2a). The convective available potential energy (CAPE) observed at Osan is 1753 J kg^{-1} and convective inhibition (CIN) is 7 J kg^{-1} prior to the precipitation event at 0600 UTC (Fig. 2b). Both CAPE and CIN are conducive to the development of deep convection. In the sounding at 0600 UTC (blue curve), temperature decreases along the dry adiabat line below 850 hPa, which is characteristic of a well-mixed ABL, and a weak inversion layer exists at the top of the ABL. Between 850 hPa and 500 hPa, the wind veers with height, indicating mid-level warming. The sounding after the precipitation event at 1200 UTC reveals that the wind near the ground is northerly and that CAPE (154 J kg^{-1}) has decreased, indicating a release of CAPE through convective precipitation.

Figure 3a shows the horizontal distribution of 9-h accumulated precipitation at 1500 UTC at the stations located in domain 4. Heavy precipitation occurred in the vicinity of Gwanak Mountain ($37^\circ 30' \text{N}$, $126^\circ 58' \text{E}$), and all three stations with 9-h accumulated precipitation greater than 80 mm were located on the windward north side of Gwanak Mountain. Hence, it is likely that orographic lifting played a role in triggering or enhancing the updraft motion. Figure 3b shows radar estimated rain rate in domain 4 at 0930 UTC. We can notice large rainfall near Gwanak Mountain and also over the sea and the mountainous area in the southeast where AWS rainfall data are not available. Precipitation commenced at 0800 UTC and lasted for approximately 5 h in the southeastern section of the metropolitan area. Intensive rainfall occurred from 0900 UTC to 1000 UTC (Fig. 3c).

Figure 4 shows enhanced infrared images from COMS over the Korean Peninsula. Deep convective cells develop in the northeastern region of Gyeonggi at 0500 UTC, and

Fig. 2 **a** Surface weather chart at 0600 UTC before the onset of convective rainfall, **b** soundings at Osan for 0600 UTC (blue) and 1200 UTC (red) on August 16, 2015. Solid and dot line in **b** indicate sounding of air temperature and dew point temperature, respectively



the Seoul metropolitan area is covered with mid-level clouds (Fig. 4a). In Seoul, there is little precipitation at this time; however, heavy precipitation (32.5 mm) occurs in the northeastern region of Gyeonggi (38°05'N, 127°16'E), and the 2-m air temperature decreased by approximately 10 K, forming a cold pool over the rainfall region. At 0800 UTC, the cloud over the metropolitan area disappeared (Fig. 4b). As strong convection developed at 0900 UTC, tall cumulonimbus cloud developed and grew to a maximum at 0930 UTC in the southeastern region of the metropolitan area (Fig. 4c, d). The temperature at the cloud top was less than -45°C which corresponds to approximately 220 hPa in the Osan sounding (Fig. 2b).

The observed 10-m wind vectors and 2-m temperature at 0500 UTC and 0800 UTC are presented in Fig. 5. Between 0400 and 0600 UTC, a cold pool formed due to the preexisting precipitation in the northeastern section of

the Gyeonggi Province, and initial northeasterly outflow from the preexisting convective storm developed. At 0500 UTC, northeasterly wind was confined to the cold pool and the wind speed over the urban areas remained low. At 0800 UTC, due to propagation of the cold pool, local 2-m air temperature decreased markedly in the northern part of the Han River, reducing convective instability. The northeast wind was stronger over the Han River due to an enhanced temperature gradient between the northern and southern sections of the Han River. Furthermore, the clearing sky over the metropolitan area at 0800 UTC (Fig. 4b) facilitated the sea breeze development to the west of the city; hence the northeasterly outflow and the westerly sea breeze converged at the center of Gwanak Mountain. The low-level convergence zone combined with the orographic lifting resulted in a strong uplift of air parcels to their level of free convection (LFC). The late afternoon heating and

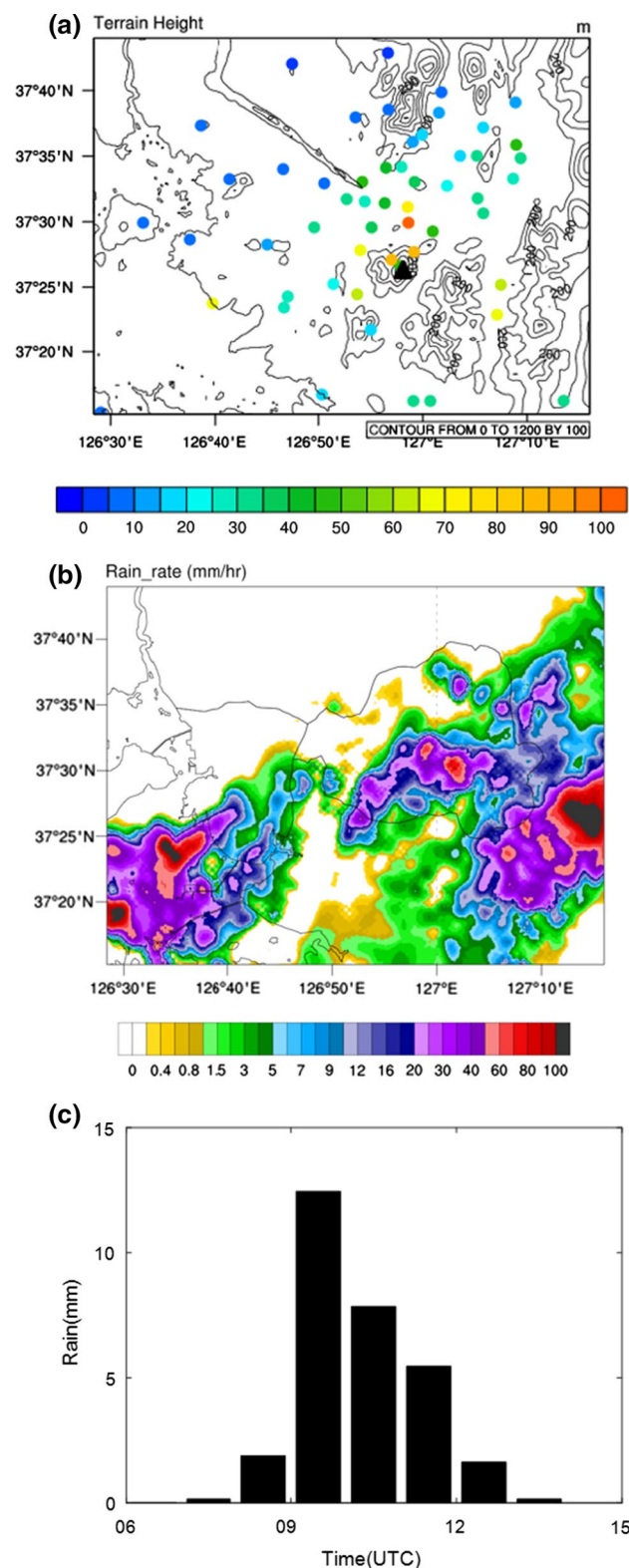


Fig. 3 **a** Horizontal distribution of 9-h accumulated rainfall (mm) (color dot) at 1500 UTC and terrain height (m) (contour), **b** horizontal distribution of radar estimate rain rate at 0930 UTC, and **c** time series of precipitation averaged over 44 analysis boxes in domain 4 on August 16, 2015. Black triangle in **a** indicates Gwanak Mountain

the breaking of the capping inversion formed strong convective cloud and generated heavy rainfall.

4 Numerical simulation and discussion

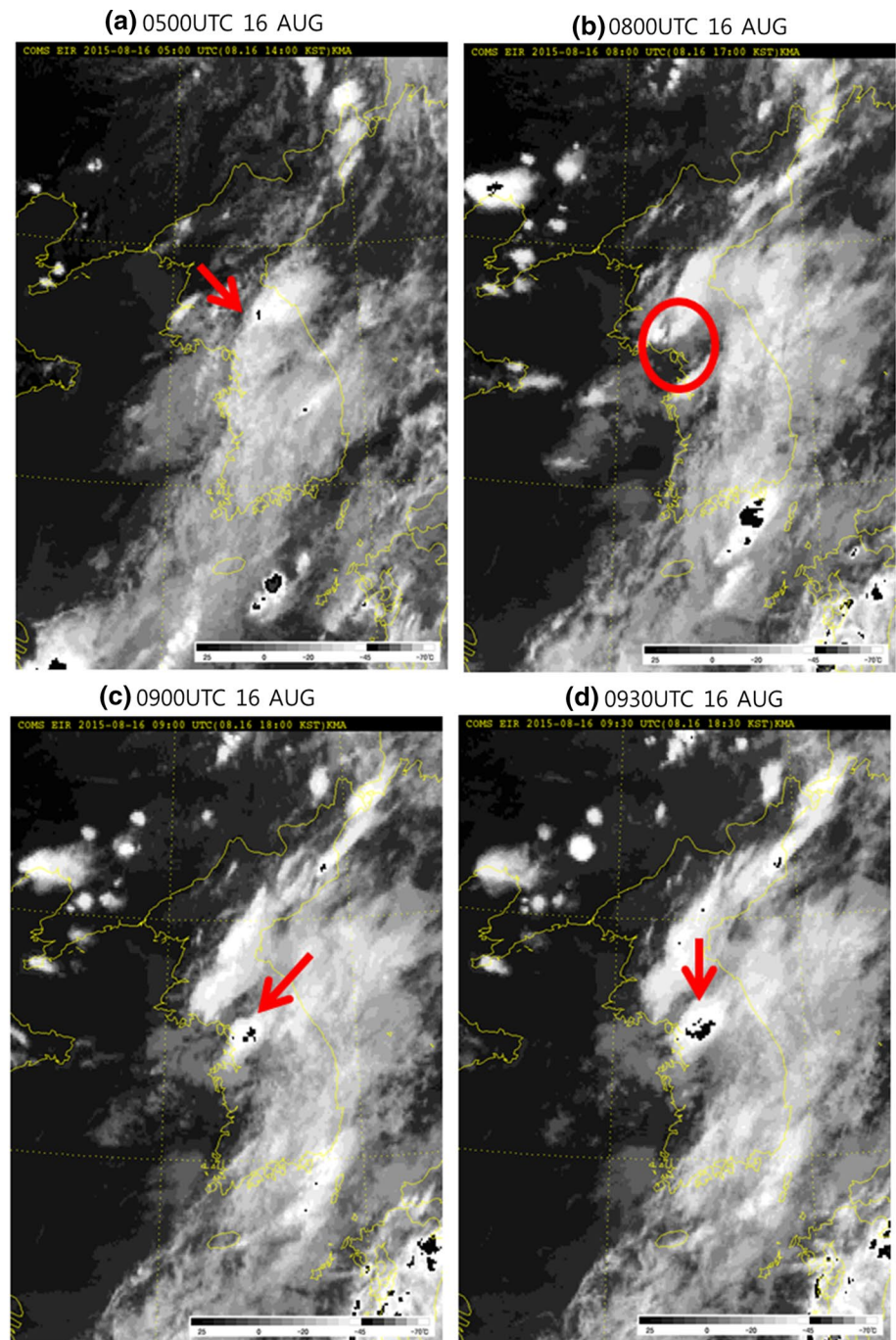
4.1 Sensitivity to initial time

Sensitivity tests were performed using four different initial times. These tests allowed us to examine the effects of micro- and mesoscale forcing on the initiation of convective rainfall under similar large-scale conditions. Although small-scale differences are apparent in 500 hPa geopotential height in domain 1 in all four simulations, large-scale features were similar in them (figure is not shown here). Here, we focus on mesoscale features to explain differences of precipitation amount in domain 4 among four experiments.

Figure 6 shows the horizontal distribution of 9-h accumulated precipitation at 1500 UTC on August 16 for the different simulations. Despite being the same case, the location and intensity of rainfall are markedly different in the four experiments. IC12, which commenced at 1200 UTC on August 15, shows good simulation of precipitation locations and precipitation amounts, although maximum rainfall (73 mm) is underestimated by 30% as compared to observations (105 mm). IC06, which had the shortest prediction time, simulates the largest average precipitation of the four experiments; however, the location of the precipitation area differs markedly from observations. This indicates that the use of a short prediction time does not guarantee a good quantitative prediction forecast for convective rainfall. Both IC18 and IC00 simulate precipitation in the eastern region of the metropolitan area; however, the precipitation amount is significantly underestimated and the precipitation area is very narrow relative to observations. Figure 7 compares the time series of average precipitation in 44 analysis boxes. Observed box average rainfall has a maximum value (12.5 mm) between 0900 UTC and 1000 UTC (Fig. 6f). Timing of the maximum value is captured by IC18, however the simulated rainfall amount in IC18 is significantly underestimated. Both IC12 and IC06 simulate maximum rainfall between 1000 UTC and 1100 UTC; whereas, IC00 simulates an earlier maximum rainfall between 0700 UTC and 0800 UTC.

To examine possible causes for the different intensity and timing of rainfall in each simulation, we analyze the domain-averaged CAPE and precipitable water (PW). Both domain-averaged CAPE and PW change over time; therefore, we compared their maximum values (Table 3) which usually occur immediately prior to precipitation. The maximum domain-averaged CAPE is moderately correlated with domain-averaged rainfall amount ($r=0.76$; r : correlation coefficient). On the other hand, domain-averaged rainfall

Fig. 4 COMS enhanced infrared image for **a** 0500 UTC, **b** 0800 UTC, **c** 0900 UTC, and **d** 0930 UTC on August 16, 2015

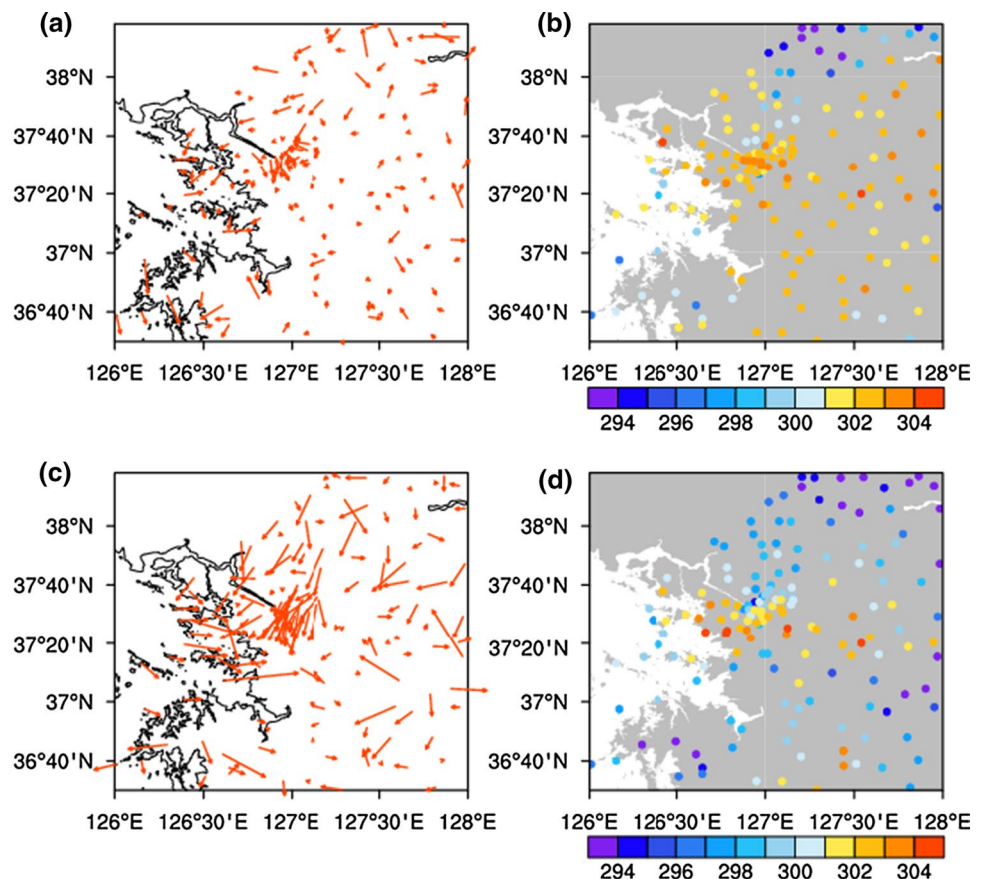


amount is highly correlated with maximum domain-averaged PW ($r=0.93$) indicating the importance of the moisture field in forecasting rainfall amount. Domain-averaged PW increases prior to the occurrence of rainfall and decreases after rainfall (Fig. 8). Dots in Fig. 8 indicate timing of peak precipitation in each experiment in Fig. 7. The amount of water vapor inside the domain is very sensitive to the transport of water vapor from outside the domain, suggesting the importance of moisture advection. This is consistent with the finding of Siqueira et al. (2009), who found that an external

source of water such as advection is required to trigger moist convection when soil is dry. We also note that IC06 is initialized with relatively high PW at 0600 UTC as compared to other simulations, which also contributes to large precipitation amount in IC06.

The horizontal distribution of simulated 10-m horizontal wind vectors is examined immediately prior to the hour of maximum precipitation (Fig. 9; for IC06, we used the first precipitation peak hour for comparison). Except for IC18, strong low-level wind convergence provides updraft motion

Fig. 5 Observed wind vector at 10 m (a, c) and air temperature (K) at 2 m (b, d) for 0500 UTC (a, b) and 0800 UTC (c, d) on August 16, 2015



for moist convection. The weak moist convection in IC18 develops in the late afternoon through the ABL top crossing the lifting condensation level (LCL) in the absence of strong low-level wind convergence. The sea breeze partly contributes to moisture transport to the urban area, increasing the domain mean PW in IC18 (Fig. 8). A relatively low supply of moisture and, hence, low PW resulted in a small amount of rainfall in IC18. The strong low-level winds in the remaining simulations were outflows driven by cold pools that formed due to earlier precipitation over the wet rural surface (Fig. 1b). Low-level outflows also transported water vapor to the dry urban area, increasing PW over the region and resulting in favorable conditions for moist convection in the late afternoon or early evening.

4.2 Impact of data assimilation

To examine the impact of data assimilation on the simulation of a convective rainfall event, we performed an additional simulation (IC06A) commencing at 0600 UTC using 3D-Var data assimilation. The IC of IC06A experiment shows a colder rural area surrounding the metropolitan area, including a cold pool in the northeastern Gyeonggi Province in domain 3 (Fig. 10a). Outflows from this cold pool are apparent in the initial wind field as shown in Fig. 10b.

The simulated results of the 9-h accumulated precipitation at 1500 UTC, 10-m wind field, and time series of precipitation amount are shown in Fig. 11a–c, respectively. The horizontal distribution of 9-h accumulated precipitation displays remarkable differences between the simulations without (Fig. 6d) and with data assimilation (Fig. 11a). Using data assimilation, the precipitation amount increased markedly and the location of the precipitation area came into good agreement with observations. Both BIAS and RMSE are reduced markedly in IC06A as compared to IC06. Furthermore, POD and HSS increased, while FAR decreased significantly (Table 4).

The IC06A 10-m wind field closely matched observations, and reproduced low-level convergence in the late afternoon (Fig. 11b). The maximum PW is considerably larger in IC06A as compared to IC06, contributing to the increase of precipitation in this simulation (Table 3). The PW increases from 41 mm to 50 mm between 0600 UTC and 0800 UTC in IC06A, indicating that water vapor is transported from surrounding rural area. Although domain-averaged PW increases over time in both IC06 and IC06A, maximum PW is larger in IC06A than in IC06, which can be attributed to the addition of water vapor on the basis of radar reflectivity data assimilation. This is consistent with previous research (e.g., Gallus and Segal 2001; Hu et al.

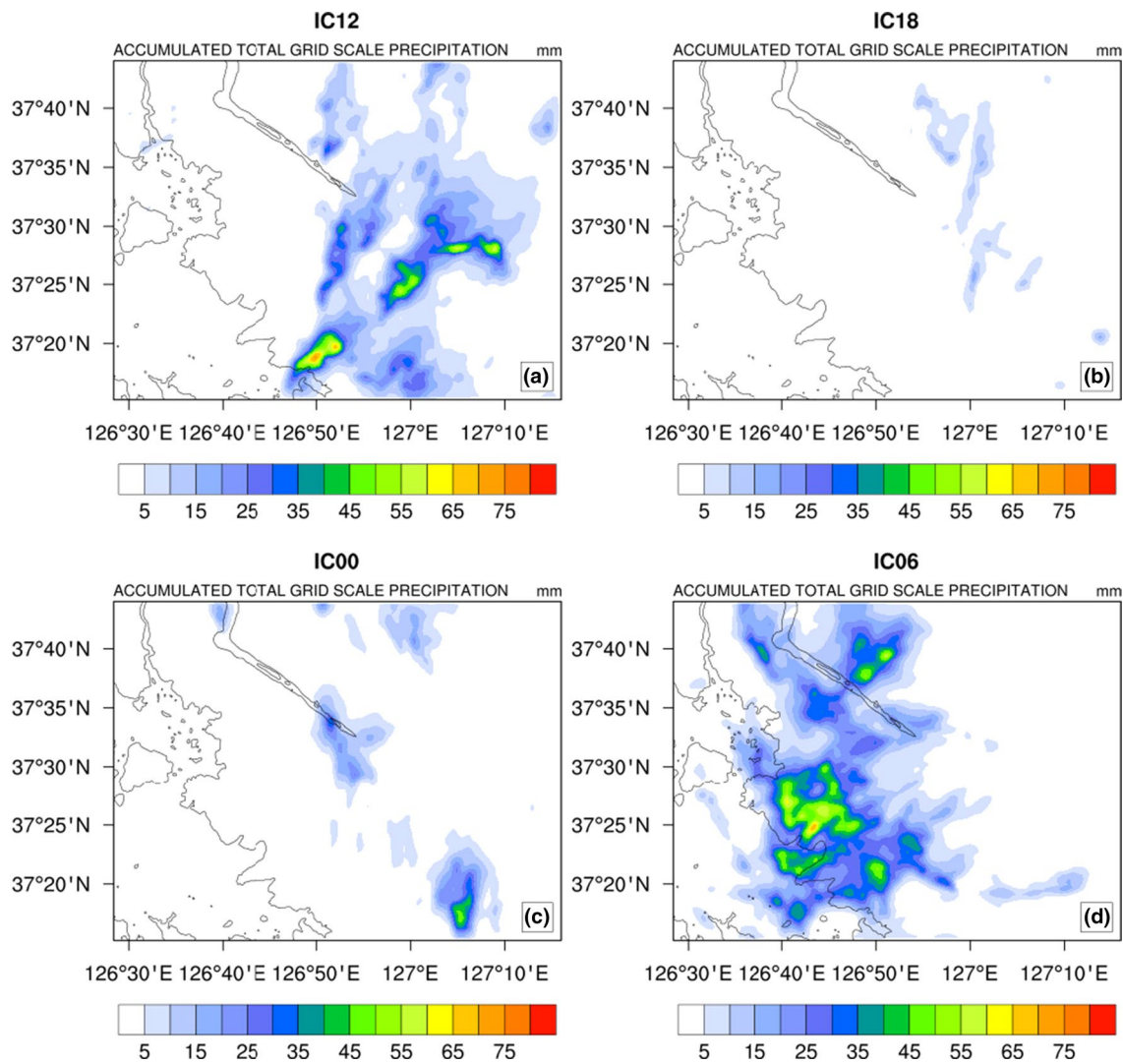


Fig. 6 Horizontal distribution of 9-h accumulated rainfall at 1500 UTC in simulation runs starting at **a** 1200 UTC on August 15 (IC12), **b** 1800 UTC on August 15 (IC18), **c** 0000 UTC on August 16 (IC00), and **d** 0600 UTC on August 16 (IC06), 2015

2006; Gao and Stensrud 2012) which found that the addition of water vapor on the basis of radar reflectivity had the greatest positive impact on the rainfall forecast. However, CAPE is much smaller in IC06A as compared to IC06. This can be attributed to increased air temperatures between 800 hPa and 350 hPa due to condensation of water vapor in IC06A. Although the domain-maximum-accumulated precipitation is larger in IC06A as compared to observations (Table 4), the domain-averaged precipitation in the analysis boxes is smaller (Figs. 3c, 11c). The low CAPE in IC06A is one possible reason for underestimation of precipitation amount. Notwithstanding, these results show that a high-resolution WRF model using radar data assimilation can predict convective storm initiation in the first few hours of the simulation and improve precipitation forecast skill in the very short-term forecasting range.

4.3 ABL and moist convection

In this section, we examine the difference in initiation time of moist convection among four simulations (IC12, IC18, IC00, and IC06) in terms of ABL growth in the model. During the day, both the ABL and LCL increase in height and often end up crossing each other, forming clouds in the afternoon (Stull 1988). Slower growth of the ABL efficiently accumulates moisture near the surface, resulting in lower LCL and LFC, and hence a faster increase in CAPE (Yin et al. 2015). However, if the growth of the ABL is too slow or the ABL is too dry, the ABL top does not cross the LCL, and moist convection cannot be triggered. Convective rainfall can occur over both dry and wet surfaces but the rainfall amount and intensity tends to be larger over wet surfaces than dry surfaces (Juang et al. 2007).

Fig. 7 Time series of precipitation averaged over 44 analysis boxes on August 16, 2015 for **a** IC12, **b** IC18, **c** IC00, and **d** IC06

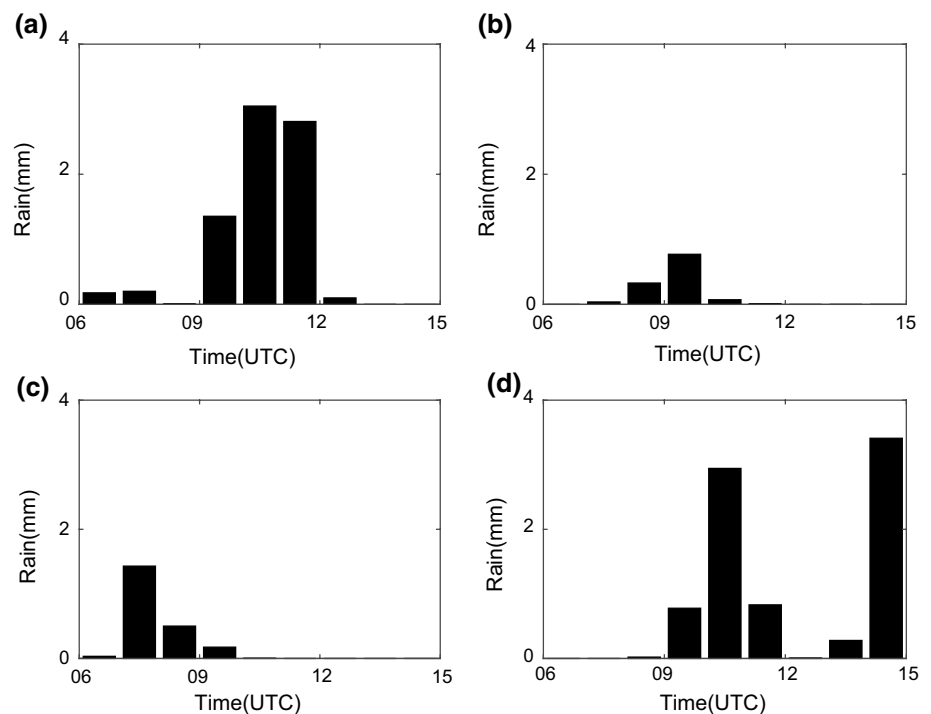


Table 3 Simulated maximum convective available potential energy (CAPE) and precipitable water (PW) averaged for domain 4 for each experiment and maximum and mean 9 h-accumulated rainfall for 1500 UTC on August 16, 2015

	IC12	IC18	IC00	IC06	IC06A
Maximum domain-averaged CAPE (J kg^{-1})	979	927	657	1142	399
Maximum domain-averaged PW (mm)	45	42	44	46	51
Maximum accumulated rainfall (mm)	73	19	49	70	124
Mean accumulated rainfall (mm)	5	1	2	9	21

Figure 12a shows the simulated ABL height compared to the mixing height from ceilometer at the JN station. In the model, the ABL height (h) is calculated as follows (Hong and Pan 1996);

$$h = \text{Rib}_{\text{cr}} \frac{\theta_{va} |U(h)|^2}{g(\theta_v(h) - \theta_s)}, \quad (8)$$

where Rib_{cr} is the critical bulk Richardson number, $U(h)$ is the horizontal wind speed at h , θ_{va} is the virtual potential temperature at the lowest level, $\theta_v(h)$ is the virtual potential temperature at h , and θ_s is the near surface temperature. The simulated ABL height represents the mixing height and hence, it is comparable with the ABL height estimated by the ceilometer. With the exception of IC06, the maximum ABL height is overestimated in the simulations. The fastest growth of the ABL occurred in IC00, while the slowest growth occurred in IC18. To understand the different behavior of ABL growth among the experiments, we examined the vertical structure of potential temperature in the lower

atmosphere at 0000 UTC (Fig. 13a). The vertical structures at 0000 UTC (IC00) were initial conditions vertically interpolated from FNL data. The inversion intensity below 1 km is strongest in IC18 and weakest in IC00. Near-surface air temperature was highest in IC00, allowing for rapid growth of ABL in this simulation. The rapid growth of ABL in IC00 is apparent in both urban and rural areas in domain 4 (figure not shown here). On the other hand, the mixing ratio in the lower atmosphere is the highest in IC12, which implies a lower LFC and, hence, explains the larger CAPE in IC12 as compared to the other simulations (Fig. 13b and Table 3).

When the ABL grows rapidly with surface heating during the daytime, both the LCL and LFC can be below the ABL top, resulting in moist convection. The initiation of moist convection over the urban area could also be triggered by the outflow boundary. Outflow from moist rural areas provides moisture, which lowers the LCL and LFC, and uplift along outflow boundary facilitates air parcels to reach the LCL and LFC. In IC12, at 0600 UTC, the ABL top crossed the LCL at the JN station (Fig. 12a, b), resulting in cloud formation and

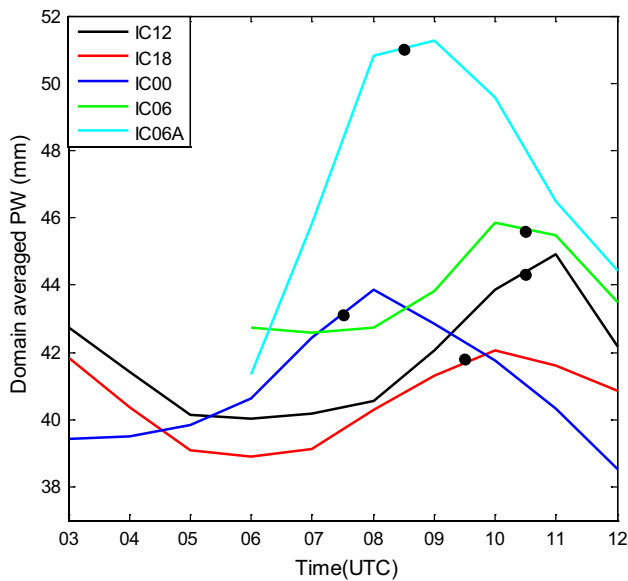


Fig. 8 Comparison of domain-averaged precipitable water (PW) with time among four experiments. Dots indicate timing of peak precipitation in Fig. 7

collapse of the ABL at 0700 UTC; however, rainfall amount was negligible at that time because of a limited supply of moisture from the dry urban surface (Figs. 7a, 8). In IC00, in which ABL growth is the fastest, the ABL top is close to the LCL at the JN station at 0600 UTC (Fig. 12). Uplift along the outflow boundary easily makes air parcels to reach the LCL and LFC, resulting in collapse of the ABL at 0800 UTC. The outflow is due to a preexisting convective storm in the rural area. The fast growth of ABL in IC00 results in earlier initiation of moist convection in the rural area than other simulations.

Slower growth of the ABL in the afternoon prevents the earlier release of CAPE in the mid-afternoon, resulting in higher CAPE in late afternoon. Except for IC06 which showed similar ABL top to that of observation, the maximum ABL top was generally higher than observed and ABL collapsed at approximately 0700 UTC. Cloud formation cools the surface below the cloud, which results in collapse of the ABL. This is one reason for lower values of CAPE in the simulations (Table 3) as compared to observation (1753 J kg^{-1}).

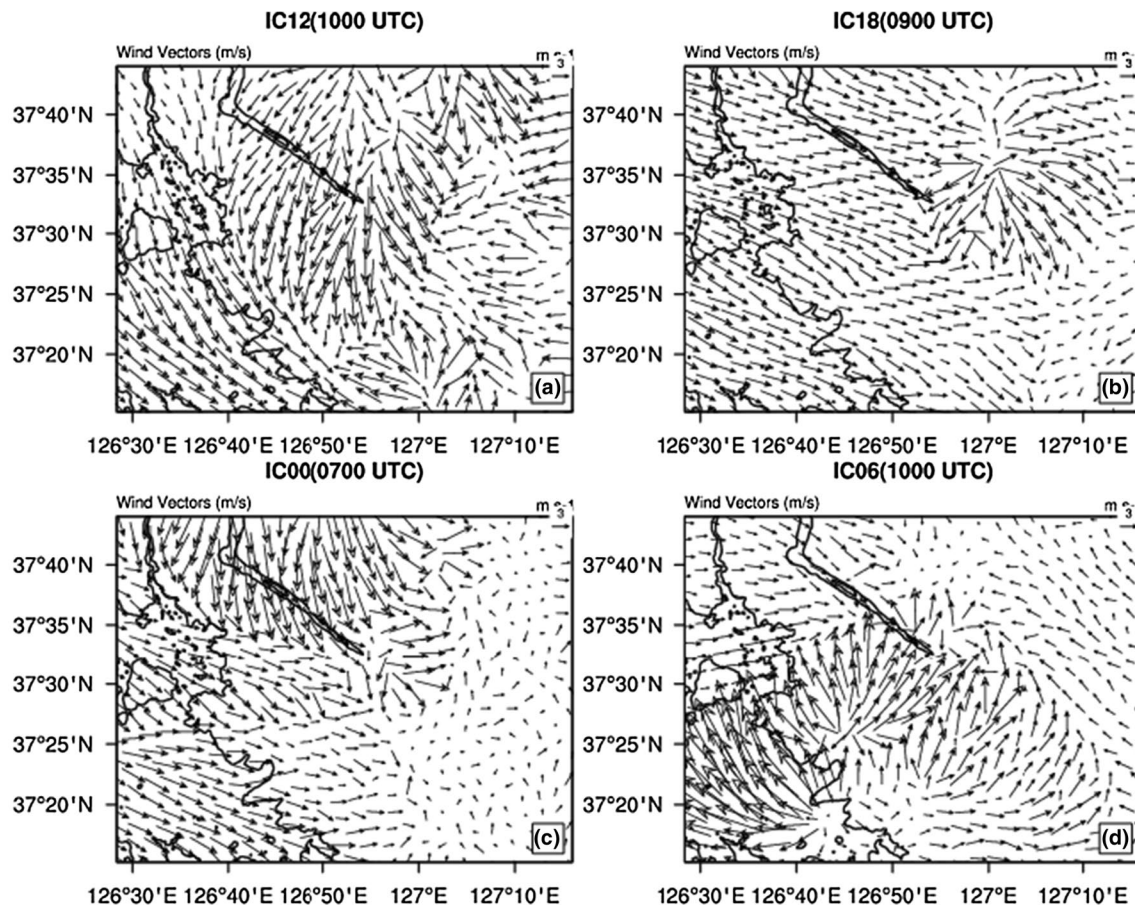


Fig. 9 Horizontal distribution of 10-m wind vectors immediately prior to the maximum precipitation hour. Time in parenthesis indicates the hour of the displayed wind vectors

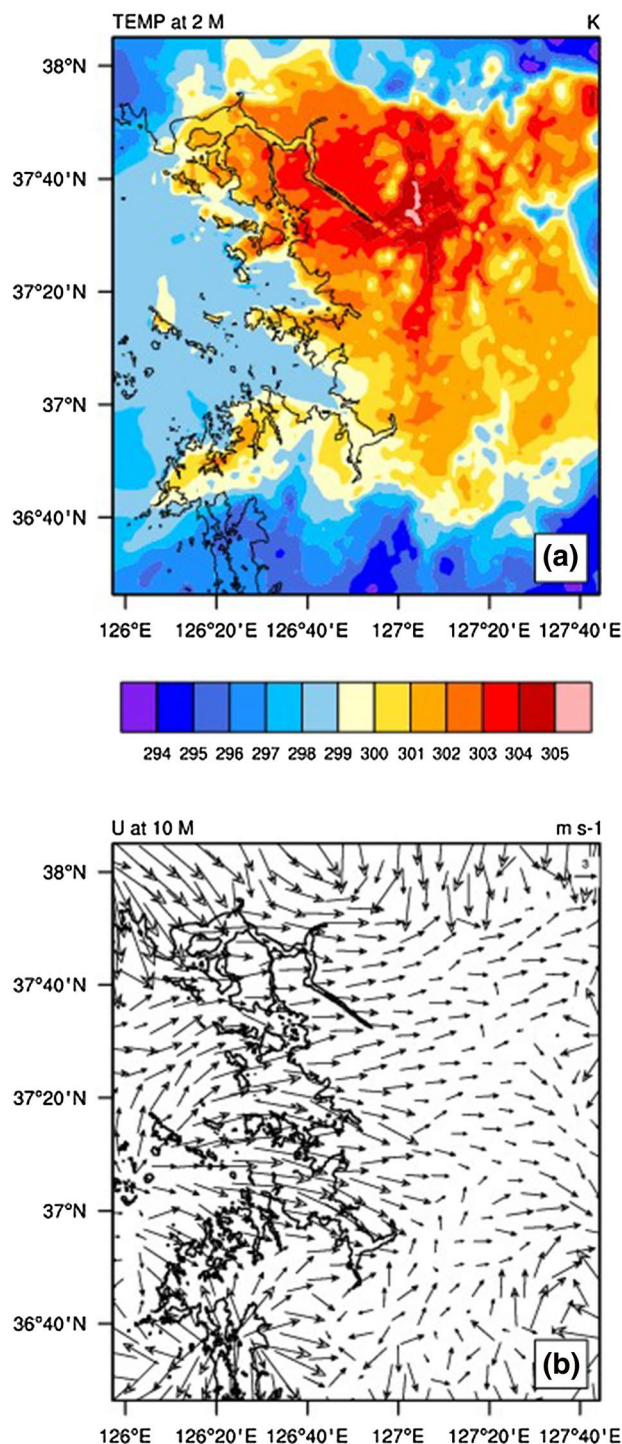


Fig. 10 Initial condition of **a** 2-m temperature and **b** 10-m wind vector for simulation using data assimilation (IC06A) in domain 3

5 Summary and conclusions

We investigated the ability of a high-resolution (500 m) numerical weather prediction (NWP) model to simulate an isolated convective precipitation event that occurred

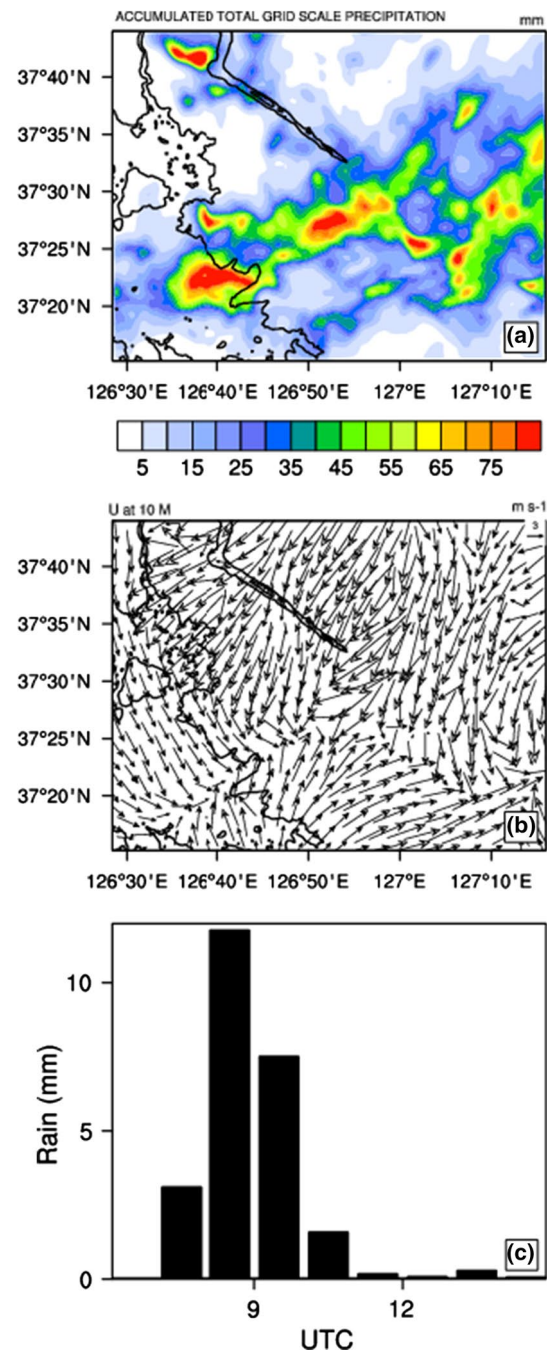
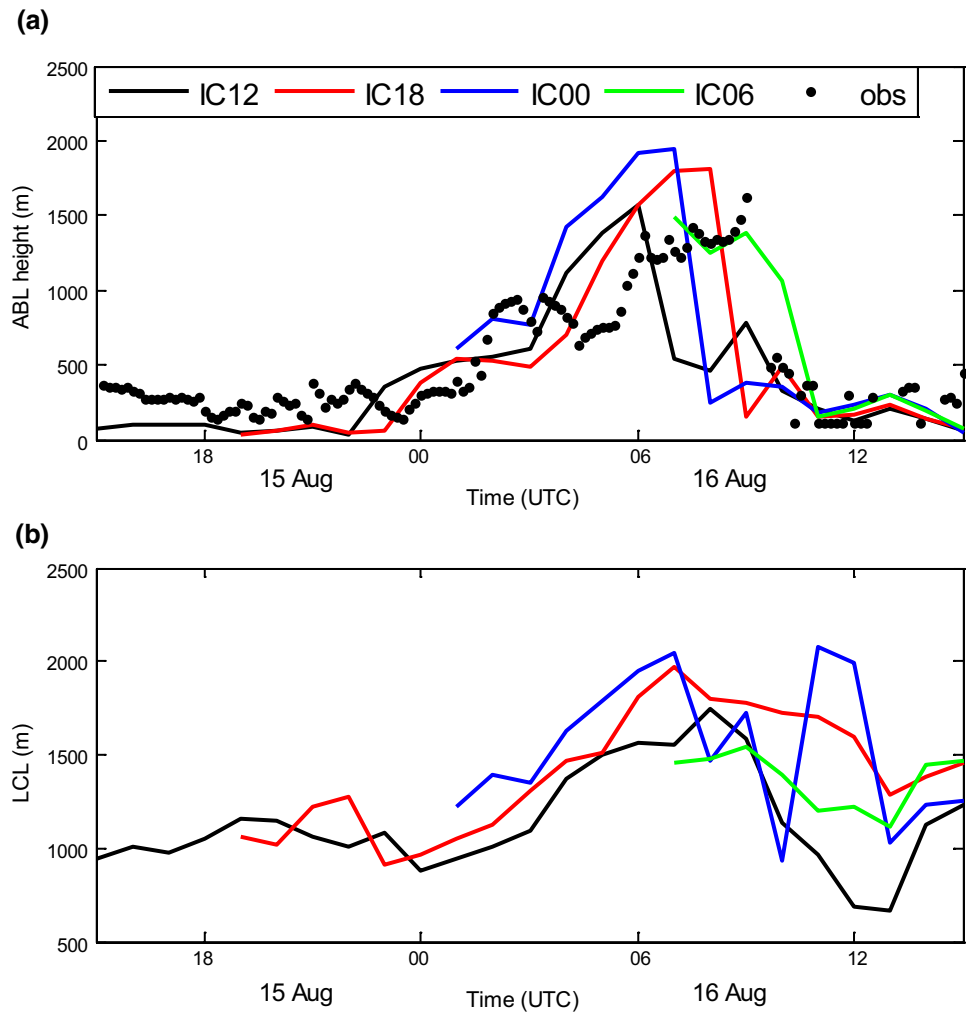


Fig. 11 **a** 9-h accumulated rainfall at 1500 UTC on August 16, **b** 10-m wind vector at 0800 UTC in domain 4 and **c** time series of precipitation averaged over 44 analysis boxes of IC06A

over the Seoul metropolitan area on August 16, 2015. Observational analysis showed that the convective rainfall developed in the presence of a mesoscale low-level wind convergence driven by a cold pool and outflows from a preexisting convective storm in the surrounding rural area in an unstable atmosphere without strong synoptic forcings.

Table 4 Scores computed on the simulated accumulated precipitation for IC06, and IC06A. ACC, POD, FBIAS, FAR, and HSS, were computed on 2×2 contingency table with a threshold of 25 mm. Thethreshold value is the median value of observed precipitation of boxes of 25 km^2 analysis boxes

Experiment	BIAS (mm)	RMSE (mm)	ACC	POD	FBIAS	FAR	HSS
IC06	-21.39	34.12	0.48	0.09	0.17	0.50	-0.01
IC06A	-5.00	19.24	0.77	0.74	0.91	0.19	0.55

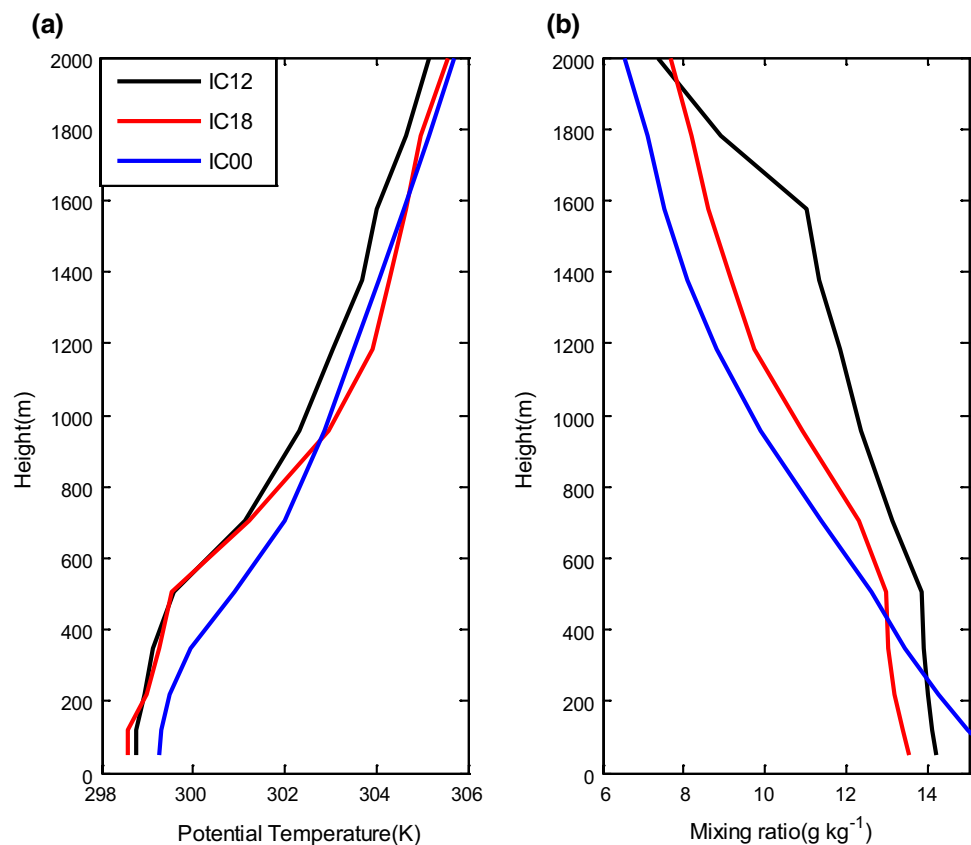
Fig. 12 Comparison of time series of **a** atmospheric boundary layer height (ABL) and **b** lifting condensation level (LCL) among simulations IC12, IC18, IC00, and IC06 compared with observation (dot) at the Jungnang (JN) station

To understand the initiation of the convective precipitation over the metropolitan area, sensitivity tests were performed using different ICs (IC12, IC18, IC00, and IC06). The QPFs varied markedly among the experiments, depending on the timing of ICs. Large rainfall amount was produced by the presence of low-level wind convergence in the late afternoon. Most simulations showed low-level wind convergence along an outflow boundary caused by a preexisting convective storm in the surrounding rural area; however, the timing and intensity of moist convective rainfall differed.

The impact of surface observation and radar data assimilation (IC06A) on simulation of a convective rainfall

event was evaluated with a focus on the accumulated rainfall amount. The simulation (IC06A) reproduced the location and amount of rainfall well; both the BIAS and RMSE were markedly reduced in IC06A as compared to IC06. Moreover, the POD and HSS increased, and the FAR decreased significantly in IC06A relative to IC06. However, simulated CAPE over the Seoul metropolitan area was reduced in IC06A, indicating that the rainfall event was not driven by high CAPE but rather by the convergence of moisture and winds. The data assimilation experiment showed that the high-resolution NWP model with adequate radar assimilation was able to predict an isolated

Fig. 13 Comparison of **a** potential temperature and **b** mixing ratio profiles between simulations IC12, IC18 and IC00 at 0000 UTC on August 16, 2015



convective precipitation event with a short lifetime (1–3 h) effectively within a spin-up period of 6 h. The success of this simulation is expected to be used as a baseline for an Observing System Simulation Experiment (OSSE) when X-band radars are added in domain 3 or 4.

The timing of moist convection was examined in terms of ABL growth. The growth of the ABL in the morning showed high variability due to a different intensity of the nocturnal inversion among the experiments. Fast growth of the ABL allowed earlier occurrence of moist convection in the urban area at the outflow boundary. In most model simulations, maximum ABL height was higher than observation and the ABL collapse occurred earlier, which contributed to the underestimation of CAPE in the late afternoon. These results highlight the importance of accurately simulating ABL growth for reasonable prediction of timing and intensity of convective precipitation. It should be noted that ABL growth is not the only factor to influence timing and intensity of convective rainfall. Mesoscale processes such as density current flow and upslope flow can also influence timing and intensity of convective storms, which will be an interesting topic for future study.

This study focused on a case study to examine the applicability of data assimilation on forecasting an isolated convective system with short lifetime. Future study is needed to evaluate the detailed performance of various

data assimilation techniques for prediction of convective storms.

Acknowledgements This subject is supported by Korea Ministry of Environment (MOE) as “Water Management Research Program”. The ceilometer data used were provided by the Weather Information Service Engine Project.

References

- Ahrens CD (2009) *Meteorology today*. Brooks/Cole, Delmont
- Arya SP (2001) *Introduction to micrometeorology*. Academic Press, San Diego
- Barker DM, Huang W, Guo YR, Bourgeois AJ, Xiao QN (2004) A three-dimensional variational data assimilation system for MM5: implementation and initial results. *Mon Weather Rev* 132:897–914. [https://doi.org/10.1175/1520-0493\(2004\)132%3c0897:ATVDAS%3e2.0.CO;2](https://doi.org/10.1175/1520-0493(2004)132%3c0897:ATVDAS%3e2.0.CO;2)
- Barker D, Huang XY, Liu Z, Auligné T, Zhang X, Rugg S, Ajjaji R, Bourgeois A, Bray J, Chen Y, Demirtas M, Guo YR, Henderson T, Huang W, Lin HC, Michalakes J, Rizvi S, Zhang X (2012) The weather research and forecasting (WRF) model’s community variational/ensemble data assimilation system: WRFDA. *Bull Am Meteorol Soc* 93:831–8843. <https://doi.org/10.1175/bams-d-11-00167.1>
- Davolio S, Buzzi A, Malguzzi P (2007) High resolution simulations of an intense convective precipitation event. *Meteorol Atmos Phys* 95:139–154. <https://doi.org/10.1007/s00703-006-0200-0>

- Ducrocq V, Richard D, Lafore JP, Orain F (2002) Storm-scale Numerical rainfall prediction for five precipitating events over France: on the importance of the initial humidity field. *Weather Forecasting* 17:1236–1256. [https://doi.org/10.1175/1520-0434\(2002\)017%3c1236:ssnrfp%3e2.0.co;2](https://doi.org/10.1175/1520-0434(2002)017%3c1236:ssnrfp%3e2.0.co;2)
- Dudhia J (1989) Numerical study of convection observed during the winter monsoon experiment using a mesoscale two-dimensional model. *J Atmos Sci* 46:3077–3107. [https://doi.org/10.1175/1520-0469\(1989\)046%3c3077:nsocod%3e2.0.co;2](https://doi.org/10.1175/1520-0469(1989)046%3c3077:nsocod%3e2.0.co;2)
- Duran DR, Wyen JA (2016) Thunderstorms do not get butterflies. *Bull Am Meteorol Soc* 97:237–243. <https://doi.org/10.1175/bams-d-15-00070.1>
- Eresmaa N, Karppinen A, Joffre SM, Rasanen J, Talvitie H. (2006) Mixing height determination by ceilometer. *Atmos Chem Phys* 6: 1485–1493. <https://doi.org/10.5194/acp-6-1485-2006>
- Findell KL, Eltahir EAB (2003a) Atmospheric controls on soil moisture-boundary layer interaction. Part I: framework development. *J Hydrometeorol* 4:552–569. [https://doi.org/10.1175/1525-7541\(2003\)004%3c0552:acosml%3e2.0.co;2](https://doi.org/10.1175/1525-7541(2003)004%3c0552:acosml%3e2.0.co;2)
- Findell KL, Eltahir EAB (2003b) Atmospheric controls on soil moisture-boundary layer interaction. Three-dimensional wind effects. *J Geophys Res* 108(D8):8385. <https://doi.org/10.1029/2001JD001515>
- Gallus WA, Segal M (2001) Impact of improved initialization of mesoscale features on convective system rainfall in 10-km Eta simulation. *Wea Forecasting* 16:680–696. [https://doi.org/10.1175/1520-0434\(2001\)016%3c0680:ioiom%3e2.0.co;2](https://doi.org/10.1175/1520-0434(2001)016%3c0680:ioiom%3e2.0.co;2)
- Gao J, Stensrud DJ (2012) Assimilation of reflectivity data in a convective-scale, cycled 3DVAR framework with hydrometeor classification. *J Atmos Sci* 69:1054–1065. <https://doi.org/10.1175/jas-d-11-0162.1>
- Hanley KE, Kirchbaum DJ, Belcher SE, Roberts NM, Leoncini G (2011) Ensemble predictability of an isolated mountain thunderstorm in a high-resolution model. *Q J Roy Meteorol Soc* 137:2124–2137. <https://doi.org/10.1002/qj.877>
- Hong SY, Lim J (2006) The WRF single-moment 6-class microphysics scheme (WSM6). *J Korean Meteorol Soc* 42:129–151
- Hong SY, Pan HL (1996) Nonlocal boundary layer vertical diffusion in a medium-range forecast model. *Mon Weather Rev* 124:2322–2339. [https://doi.org/10.1175/1520-0493\(1996\)124%3c2322:nblvdi%3e2.0.co;2](https://doi.org/10.1175/1520-0493(1996)124%3c2322:nblvdi%3e2.0.co;2)
- Hu M, Xue M, Brewster K (2006) 3DVAR and cloud analysis with WSR-88D Level-II data for the prediction of the Fort Worth tornadic thunderstorms. Part I: cloud analysis and its impact. *Mon Wea Rev* 134:675–698
- Juang JY, Porporato A, Stoy PC, Siqueira MS, Oishi AC, Detto M, Kim HS, Katul GG (2007) Hydrologic and atmospheric controls on initiation of convective precipitation events. *Water Resour Res* 43:W03421. <https://doi.org/10.1029/2006WR004954>
- Kain JS, Fritsch JM (1993) Convective parameterization for mesoscale models. The Kain-Fritsch scheme. In: Emanuel KA and Raymond DJ (eds) *The representation of cumulus convection in numerical models*. *Am Meteorol Soc*, pp 165–170. https://doi.org/10.1007/978-1-935704-13-3_16
- Kusaka H, Kondo H, Kikegawa Y, Kimura F (2001) A simple single-layer urban canopy model for atmospheric models: comparison with multi-layer and slab models. *Bound-layer Meteorol* 101:329–358. <https://doi.org/10.1023/a:1019207923078>
- Lee JH, Lee HH, Choi Y, Kim HW, Lee DK (2010) Radar data assimilation for the simulation of mesoscale convective systems. *Adv Atmos Sci* 27(5):1025–1042. <https://doi.org/10.1007/s00376-010-9162-8>
- Lorenz E (1969) The predictability of a flow which possesses many scales of motion. *Tellus* 21(3):289–330. <https://doi.org/10.1111/j.2153-3490.1969.tb00444.x>
- Min KH, Choo SH, Lee GW, Lee DH (2015) Evaluation of WRF cloud microphysics schemes using radar observations. *Weather Forecasting* 30(6):1571–1589. <https://doi.org/10.1175/waf-d-14-00095.1>
- Mitchell K (2005) The community Noah Land-Surface Model (LSM). ftp://ftp.emc.ncep.noaa.gov/mmb/gcp/ldas/noahlsn/ver_2.7.1. Accessed 16 Jan 2014
- Mlawer EJ, Taubman SJ, Brown PD, Iacono MJ, Clough SA (1997) Radiative transfer for inhomogeneous atmosphere: RRTM, a validated correlated k-model for the long-wave. *J Geophys Res* 102(D14):16663–166682. <https://doi.org/10.1029/97jd00237>
- Munkel C, Eresmaa N, Rasanen J, Karppinen A (2007) Retrieval of mixing height and dust concentration with lidar ceilometer. *Bound-Layer Meteorol* 124:117–128. <https://doi.org/10.1007/s10546-006-9103-3>
- NCEP (2015) NCEP GDAS/FNL 0.25 degree global tropospheric analysis and forecast grids. <https://doi.org/10.5065/D65Q4T4Z>. Accessed 10 Sep 2015
- NIMR (2014) Construction of input data for WRF-UCM using GIS and its operating method. NIMR-TN-2014-016, NIMR
- Park JY, Suh MS (2015) Improvement of MODIS land cover classification over the Asia-Oceania region. *Korean J Remote Sens* 31(2):51–64. <https://doi.org/10.7780/kjrs.2015.31.2.1>
- Park, Park SH, Chae JH, Choi MH, Song Y, Kang M, Roh JW (2017) High-resolution urban observation network for user-specific meteorological information service in the Seoul Metropolitan area, South Korea. *Atmos Meas Tech* 10:1575–1594. <https://doi.org/10.5194/amt-10-1575-2017/>
- Parrish DF, Derber JC (1992) The National Meteorological Center's spectral statistical-interpolation analysis system. *Mon Weather Rev* 120:1747–1763. [https://doi.org/10.1175/1520-0493\(1992\)020%3c1747:tnmcss%3e2.0.co;2](https://doi.org/10.1175/1520-0493(1992)020%3c1747:tnmcss%3e2.0.co;2)
- Reuter HI, Nelson A, Jarvis A (2007) An evaluation of void filling interpolation methods for SRTM data. *Int J Geogr Inf Sci* 21(9):983–1008. <https://doi.org/10.1080/136588106>
- Shin HH, Hong SY (2015) Representation of the subgrid-scale turbulent transport in convective boundary layers at Gray-zone resolutions. *Mon Weather Rev* 143:250–271. <https://doi.org/10.1175/mwr-d-14-00116.1>
- Siqueira M, Katul G, Porporato A (2009) Soil moisture feedbacks on convection triggers: the role of soil-plant hydrodynamics. *J Hydrometeorol* 10(1):96–112. <https://doi.org/10.1175/2008JHM1027.1>
- Skamarock WC, Klemp JB, Dudhia J, Gill DO, Barker DM, Duda MG, Huang XY, Wang W, Powers JG (2008) A description of the advance research WRF version 3. NCAR technical note, NCAR/TN-475+STR
- Stull RB (1988) *An introduction to boundary layer meteorology*. Kluwer Academic Publishers, London
- Xiao Q, Sun, J (2007) Multiple-radar data assimilation and short-range quantitative precipitation forecasting of a squall line observed during IHOP_2002. *Mon Weather Rev* 135:3381–3404. <http://doi.org/10.1175/MWR3471.1>
- Sun J, Xue M, Wilson JW, Zawadzki I, Ballard SP, Onville-Hooimeyer J, Joe P, Barker DM, Li PW, Golding B, Xu M, Pinto J (2014) Use of NWP for nowcasting convective precipitation. *Bull Am Meteorol Soc* 95:409–426. <https://doi.org/10.1175/bams-d-11-00263.1>
- Tsaknakis G, Papayannis A, Kokkalis P, Amiridis V, Kambezidis HD, Mamouri RE, Georgoussis G, Avdikos G (2011) Inter-comparison of lidar and ceilometer retrievals for aerosol and planetary boundary layer profiling over Athens, Greece. *Atmos Measure Tech* 4:1261–1273. <https://doi.org/10.5194/amt-4-1261-2011>
- Walser A, Lüthi D, Schär C (2004) Predictability of precipitation in a cloud-resolving model. *Mon Weather Rev* 132:560–577. [https://doi.org/10.1175/1520-0493\(2004\)132%3c0560:popia%3e2.0.co;2](https://doi.org/10.1175/1520-0493(2004)132%3c0560:popia%3e2.0.co;2)

- Wang H, Sun J, Fan S, Huang XY (2013) Indirect assimilation of radar reflectivity with WRF 3D-Var and its impact on prediction of four summertime convective events. *J Appl Meteorol Climatol* 52:889–902. <https://doi.org/10.1175/jamc-d-12-0120.1>
- Wilks DS (2006) *Statistical methods in the atmospheric sciences*, 2nd edn. Academic Press, San Diego
- Yin J, Albertson JD, Rigby JR, Porporato A (2015) Land and atmospheric controls on initiation and intensity of moist convection: CAPE dynamics and LCL crossings. *Water Resour Res* 51:8476–8493. <https://doi.org/10.1002/2015WR017286>
- Zhang F, Odins AM, Nielsen-Gammon JW (2006) Mesoscale predictability of an extreme warm-season precipitation event. *Wea Forecasting* 21:149–166. <https://doi.org/10.1175/waf909.1>

Publisher's Note Springer Nature remains neutral with regard to jurisdictional claims in published maps and institutional affiliations.